AIAA AVIATION Forum
5-9 June 2017, Denver, Colorado
47th AIAA Fluid Dynamics Conference

AIAA 2017-4312

Sensitivity analysis for the control of oblique shock wave/laminar boundary layer interactions at Mach 5.92

Nathaniel Hildebrand[*], Anubhav Dwivedi[*], Joseph W. Nichols[†], and Graham V. Candler[‡]
University of Minnesota, Minneapolis, MN, 55455, USA

Mihailo R. Jovanović[§]
University of Southern California, Los Angeles, CA, 90089, USA

At a transitional Reynolds number, we examine the instability of an oblique shock wave impinging on a hypersonic laminar boundary layer. Using global stability analysis we identify the critical oblique shock angle at which the 2D laminar flow first becomes unstable to 3D perturbations. The non-dimensional spanwise wavenumber selected at this bifurcation is $\beta = 0.25$. Long streamwise streaks that originate in the shear layer on top of the recirculation bubble are present in the unstable stationary global mode. We compute the adjoint eigenmodes to understand how upstream fluctuations affect the direct global modes of the system, and we see that the least stable stationary global mode is receptive to forcing inside the boundary layer and along the oblique shock wave. The wavemaker, which is defined as the sensitivity of an eigenvalue to base flow modification, is then computed. For every case, the wavemaker resides in the recirculation bubble, but it shifts towards the reattachment point as the incident shock angle increases. A calculation of the Görtler number about several 2D base flows revealed that a centrifugal instability cannot be the sole reason for bifurcation.

I. Introduction

High-speed flows over complex geometries are typically characterized by shock wave/boundary layer interactions (SWBLI) and have been the subject of many experimental and numerical investigations.[1] The strong adverse pressure gradient created by an oblique shock wave impinging on a laminar boundary layer can cause it to separate from the wall. Boundary layer separation results in the formation of a recirculation bubble that can become three-dimensional (3D) and unsteady. Thus, SWBLI provides a mechanism for transition to turbulence that is different from the usual pathways based on boundary layer instabilities initiated by Mack modes.[2,3] Once a hypersonic boundary layer has transitioned, the skin friction and heat flux increase by a factor of five to six.[4] Additionally, in the case of SWBLI, self-sustained oscillations supported by the recirculation bubble may produce unsteady loads.

The interaction of a laminar boundary layer with shock waves has been studied using stability theory and numerical simulations at subsonic and supersonic conditions. For an incompressible separation bubble, Theofilis et al.[5] and Rodriguez & Theofilis[6] determined that a region of positive skin-friction inside the primary bubble results in a bifurcation from two-dimensional (2D) flow to a 3D steady state. Robinet[7] used direct numerical simulations (DNS) of a compressible SWBLI to show that a steady 2D flow bifurcates to a 3D state in different ways as the oblique shock angle increases depending on the spanwise extent of the computational domain. For small spanwise domain sizes, the SWBLI bifurcated into a steady 3D flow with an increase in the shock angle. As the oblique shock angle increases yet further, the flow bifurcated into an unsteady 3D state. For sufficiently large spanwise extents, however, the 2D flow bifurcated directly to a 3D

---

[*] Graduate Research Assistant, UMN Aerospace Engineering and Mechanics, AIAA Student Member.
[†] Assistant Professor, UMN Aerospace Engineering and Mechanics, AIAA Member.
[‡] Russell J. Penrose and McKnight Presidential Professor, UMN Aerospace Engineering and Mechanics, AIAA Fellow.
[§] Professor, USC Electrical Engineering, IEEE Senior Member.

Copyright © 2017 by the American Institute of Aeronautics and Astronautics, Inc.
All rights reserved.

unsteady state. Global stability analysis identified an unstable stationary mode, which explained the first bifurcation to a steady 3D flow.

There are currently two explanations for the source of low-frequency unsteadiness in an oblique shock wave/turbulent boundary layer interaction. On one hand, several studies show how shock motion is linked to the turbulence of an incoming boundary layer. Although not directly related to low-frequency unsteadiness, Erengil & Dolling[8] convey in their experimental work on compression ramps at Mach 5 how small-scale jittery motion of the shock wave is affected by the passage of fluctuations in static quantities across it. Ünalmis & Dolling[9] propose low-frequency unsteadiness is influenced by the thickening and thinning of the turbulent boundary layer upstream. More recently, Ganapathisubramani et al.[10] show in their experimental studies that shock motion is affected by long upstream low-speed and high-speed streaks. Wu & Martin[11] saw a significant correlation between motion of the separation line surrogate and fluctuations in the upstream boundary layer with DNS. This agrees well with previous work.[10] However, the correlation was lower when tested with the actual separation line. In the large eddy simulations of Touber & Sandham,[12] low-frequency oscillations are observed when no coherent structures exist upstream. Nichols et al.[14] show that turbulent SBLI can be interpreted as a forced weakly damped oscillator. Lastly, Priebe & Martin[13] suggest that Görtler instability is important for turbulent boundary layers over a compression ramp.

An extensive amount of work suggests the internal mechanism within the recirculation bubble is responsible for the unsteadiness. Dupont et al.[15] points to coherence between wall pressure fluctuations at the foot of the reflected shock and in the reattachment zone for a turbulent SWBLI. This corresponds to the breathing character of the separation bubble. A simple model based on entrainment characteristics of the shear layer as well as the mass recharge within the separation bubble has been proposed.[16] This model describes the unsteady motion of the reattachment point. Pirozzoli & Grasso[17] developed an alternative mechanism for unsteadiness driven by resonance, which involves the interaction of large structures with the incident shock. They thought this would produce acoustic disturbances that travel upstream to the separation point and lead to the low-frequency motion of the reflected shock. Studies by Touber & Sandham[12] as well as Sansica et al.[18] show there is no need for upstream forcing to obtain an unsteady response. However, they also reveal that upstream disturbances do provide a broad source of unsteady low-frequency motion. In a recent review, Clemens & Narayanaswamy[19] argue the upstream and internal mechanism are always active independent of the interaction strength.

Literature related to an oblique shock wave impinging on a laminar boundary layer at hypersonic speeds is sparse. Benay et al.[20] performed a study of SWBLI in a hollow cylinder flare model at Mach 5. A local linear stability analysis complemented this experimental and numerical investigation. For this flow configuration, oblique modes are the most unstable. More recently, Sandham et al.[21] carried out a numerical and experimental study on SWBLI at Mach 6. It is suggested that the transition process develops from second or Mack mode instabilities superimposed on streamwise streaks.

Our focus in this work is to more closely examine the bifurcation of an initially 2D flow to a 3D steady state that occurs for an oblique shock wave/laminar boundary layer interaction at Mach 5.92. The spanwise wavenumber selected at this bifurcation is characterized with global stability analysis about 2D base flows. The US3D hypersonic flow solver[22] is used to calculate the steady base flows. We compute the adjoint eigenmodes to understand how upstream fluctuations affect the direct global modes of the system. This can help explain the impact of turbulence on a SWBLI and the global modes specifically. The sensitivity of an eigenvalue to base flow modification or the wavemaker is calculated using direct and adjoint information. This reveals the spatial origin of the stability modes. We compute the Görtler number associated with curved streamlines taken from the DNS base flows to assess the possibility of centrifugal instability.[13]

II. Problem formulation

A. Flow configuration

We consider an oblique shock wave/laminar boundary layer interaction for this study. The flow configuration is depicted in Figure 1. We set the freestream Mach number, temperature, and pressure to the values of $M_\infty = 5.92$, $T_\infty = 53.06$ K, and $p_\infty = 308.2$ Pa, respectively. These values exactly match experiments performed in the ACE Hypersonic Wind Tunnel at Texas A&M University.[23] We use a Reynolds number of $Re = \rho_\infty U_\infty \delta^* / \mu_\infty = 9660$, based on the undisturbed boundary layer displacement thickness δ^* at the inlet. This corresponds to a unit Reynolds number of 4.6×10^6 m^{-1} close to transition. Here, ρ_∞, U_∞, and μ_∞ denote the freestream density, velocity, and dynamic viscosity, respectively. Note that the freestream values are taken upstream of the bow shock and the incident shock. To enable a comprehensive analysis about the stability of this flow field, we simulate a range of incident shock angles θ from 12 to 13.4 degrees. We utilize a Cartesian coordinate system in this study with x, y, and z denoting the streamwise, wall-normal, and spanwise directions, respectively.

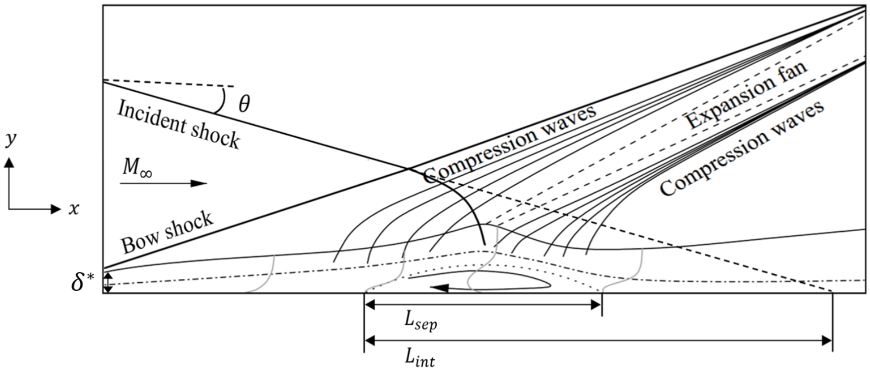

Figure 1: A detailed schematic adapted from Robinet[7] of our 2D computational domain. Here L_{sep} and L_{int} denote the separation and interaction lengths, respectively.

B. Governing equations

The compressible Navier-Stokes equations are used to mathematically model the dynamics of an oblique shock wave/laminar boundary layer interaction at hypersonic speeds. These equations govern the evolution of the system state $\boldsymbol{q} = [p;\ \boldsymbol{u}^{\mathrm{T}};\ s]^{\mathrm{T}}$, where p, $\boldsymbol{u}$, and s are the fluid pressure, velocity, and entropy, respectively.[24,25] After non-dimensionalization with respect to the displacement thickness δ^*, freestream velocity U_∞, density ρ_∞, and temperature T_∞, these equations are

$$\frac{\partial p}{\partial t} + \boldsymbol{u}\cdot\boldsymbol{\nabla}p + \rho c^2 \boldsymbol{\nabla}\cdot\boldsymbol{u} = \frac{1}{Re}\left[\frac{1}{M_\infty^2 Pr}\boldsymbol{\nabla}\cdot(\mu\boldsymbol{\nabla}T) + (\gamma-1)\phi\right], \tag{1a}$$

$$\frac{\partial \boldsymbol{u}}{\partial t} + \frac{1}{\rho}\boldsymbol{\nabla}p + \boldsymbol{u}\cdot\boldsymbol{\nabla}\boldsymbol{u} = \frac{1}{Re}\frac{1}{\rho}\boldsymbol{\nabla}\cdot\boldsymbol{\tau}, \tag{1b}$$

$$\frac{\partial s}{\partial t} + \boldsymbol{u}\cdot\boldsymbol{\nabla}s = \frac{1}{Re}\frac{1}{\rho T}\left[\frac{1}{(\gamma-1)M_\infty^2 Pr}\boldsymbol{\nabla}\cdot(\mu\boldsymbol{\nabla}T) + \phi\right]. \tag{1c}$$

For an ideal fluid, the density ρ and temperature T are related to pressure p through the equation of state $\gamma M_\infty^2 p = \rho T$. We define the Mach number $M_\infty = U_\infty/c_\infty$, where $c_\infty = \sqrt{\gamma p_\infty/\rho_\infty}$ is the speed of sound in the freestream. Further, $\gamma = 1.4$ is the assumed constant ratio of specific heats.

We define entropy as $s = \ln(T)/[(\gamma-1)M_\infty^2] - \ln(p)/(\gamma M_\infty^2)$ so that $s = 0$ when $p = 1$ and $T = 1$. The viscous stress tensor $\boldsymbol{\tau}$ can be written in terms of the identity matrix I, velocity vector $\boldsymbol{u}$, and dynamic viscosity μ to yield the following expression

$$\boldsymbol{\tau} = \mu[\boldsymbol{\nabla}\boldsymbol{u} + (\boldsymbol{\nabla}\boldsymbol{u})^{\mathrm{T}} - \frac{2}{3}(\boldsymbol{\nabla}\cdot\boldsymbol{u})I]. \tag{2}$$

The viscous dissipation is defined as $\phi = \boldsymbol{\tau} : \boldsymbol{\nabla}\boldsymbol{u}$. Note the operator $:$ represents a scalar or double dot product between two tensors. We set $\lambda/\mu = -2/3$ with λ denoting the second viscosity coefficient. In order to compute the dynamic viscosity μ, we used Sutherland's law with $T_s = 110.3$ K as follows

$$\mu(T) = T^{3/2}\frac{1 + T_s/T_\infty}{T + T_s/T_\infty}. \tag{3}$$

The Prandtl number is set to a constant value $Pr = \mu(T)/\kappa(T) = 0.72$, where $\kappa(T)$ is the coefficient of heat conductivity. We can recast system (1) into the form $\partial \boldsymbol{q}/\partial t = F(\boldsymbol{q})$, where F is the differential non-linear Navier-Stokes operator.

C. Linearized model

To investigate the behavior of small fluctuations about various base flows, we linearize system (1) by decomposing the state variables $\boldsymbol{q} = \bar{\boldsymbol{q}} + \boldsymbol{q}'$ into steady and fluctuating parts. By keeping only the first-order terms in $\boldsymbol{q}'$, we arrive at the linearized Navier-Stokes equations

$$\begin{aligned}\frac{\partial p'}{\partial t} + \bar{\boldsymbol{u}} \boldsymbol{\cdot} \boldsymbol{\nabla} p' + \boldsymbol{u}' \boldsymbol{\cdot} \boldsymbol{\nabla} \bar{p} + \bar{\rho}\bar{c}^2 \boldsymbol{\nabla} \boldsymbol{\cdot} \boldsymbol{u}' + \gamma(\boldsymbol{\nabla} \boldsymbol{\cdot} \bar{\boldsymbol{u}}) p' = \frac{1}{Re}\bigg\{ & \frac{1}{M_\infty^2 Pr} \boldsymbol{\nabla} \boldsymbol{\cdot} (\bar{\mu} \boldsymbol{\nabla} T') \\ & + (\gamma - 1)\big[\bar{\boldsymbol{\tau}} : \boldsymbol{\nabla} \boldsymbol{u}' + \boldsymbol{\tau}' : \boldsymbol{\nabla} \bar{\boldsymbol{u}}\big]\bigg\},\end{aligned} \tag{4a}$$

$$\frac{\partial \boldsymbol{u}'}{\partial t} + \frac{1}{\bar{\rho}} \boldsymbol{\nabla} p' - \frac{\rho'}{\bar{\rho}^2} \boldsymbol{\nabla} \bar{p} + \bar{\boldsymbol{u}} \boldsymbol{\cdot} \boldsymbol{\nabla} \boldsymbol{u}' + \boldsymbol{u}' \boldsymbol{\cdot} \boldsymbol{\nabla} \bar{\boldsymbol{u}} = \frac{1}{Re}\bigg\{\frac{1}{\bar{\rho}} \boldsymbol{\nabla} \boldsymbol{\cdot} \boldsymbol{\tau}' - \frac{\rho'}{\bar{\rho}^2} \boldsymbol{\nabla} \boldsymbol{\cdot} \bar{\boldsymbol{\tau}}\bigg\}, \tag{4b}$$

$$\begin{aligned}\frac{\partial s'}{\partial t} + \bar{\boldsymbol{u}} \boldsymbol{\cdot} \boldsymbol{\nabla} s' + \boldsymbol{u}' \boldsymbol{\cdot} \boldsymbol{\nabla} \bar{s} = \frac{1}{Re}\frac{1}{\bar{\rho}\bar{T}}\bigg\{ & \frac{1}{(\gamma - 1) M_\infty^2 Pr}\bigg[\boldsymbol{\nabla} \boldsymbol{\cdot} (\bar{\mu} \boldsymbol{\nabla} T') - \frac{p'}{\bar{p}} \boldsymbol{\nabla} \boldsymbol{\cdot} (\bar{\mu} \boldsymbol{\nabla} \bar{T})\bigg] \\ & + \bar{\boldsymbol{\tau}} : \boldsymbol{\nabla} \boldsymbol{u}' + \boldsymbol{\tau}' : \boldsymbol{\nabla} \bar{\boldsymbol{u}} - \frac{p'}{\bar{p}} \bar{\boldsymbol{\tau}} : \boldsymbol{\nabla} \bar{\boldsymbol{u}}\bigg\}.\end{aligned} \tag{4c}$$

Here the overbars and primes denote the base flow and fluctuating parts, respectively. We linearize the equation of state to obtain $\rho'/\bar{\rho} = p'/\bar{p} - T'/\bar{T}$. The expression $T' = (\gamma - 1) M_\infty^2 (\bar{T} s' + p'/\bar{\rho})$ comes from linearizing the definition of entropy and substituting in the equation of state. We neglect fluctuations in the dynamic viscosity or set $\mu' = 0$. This assumption is reasonable due to the fact that μ' is significantly smaller than the other fluctuating quantities.

Global modes of the linear system (4) take the form

$$\boldsymbol{q}'(x, y, z, t) = \hat{\boldsymbol{q}}(x, y) e^{i(\beta z - \omega t)}, \tag{5}$$

where β is the non-dimensional spanwise wavenumber and ω is the temporal frequency. We can represent system (4) abstractly as equation (6a). Furthermore, the Jacobian operator given by $A = \partial F/\partial \boldsymbol{q}|_{\bar{\boldsymbol{q}}}$ corresponds to the linearization of the Navier-Stokes operator F about the base flow $\bar{\boldsymbol{q}}$. Now an eigenvalue problem of the form $A\hat{\boldsymbol{q}} = -i\omega\hat{\boldsymbol{q}}$ can be solved numerically.

In addition to the eigenvalues and their associated eigenfunctions, we are also interested in their sensitivity to slight changes in the base flow.[26] We define the spatial region of maximum sensitivity as the wavemaker[27,28] because it corresponds to the location where an instability originates. The wavemaker can be computed after solving the adjoint problem. If $\boldsymbol{q}^+$ represents the adjoint state variables, and we define A^+ as the adjoint of operator A, then we arrive at system (6b). Notice the equations below are similar

$$\frac{\partial \boldsymbol{q}'}{\partial t} = A\boldsymbol{q}', \quad \frac{\partial \boldsymbol{q}^+}{\partial t} = A^+ \boldsymbol{q}^+. \tag{6a,b}$$

Thus, the direct and adjoint problems can be solved in an identical manner. Eigenvalue spectra computed with the direct and adjoint equations should be conjugate symmetric by construction. The corresponding eigenfunctions are expected to be significantly different. As we will see later, the adjoint perturbations travel upstream instead of downstream with the flow. We calculated the adjoint operator A^+ by applying integration by parts to system (4).

D. Numerical methods

For the base flow calculations, we solve the compressible Navier-Stokes equations in conservative form.[29] A stable low-dissipation scheme based upon the kinetic energy consistent (KEC) method developed by Subbareddy and Candler[30] is implemented for the inviscid flux computation. In this numerical method, we split the inviscid flux into a symmetric (or non-dissipative) portion and an upwind (or dissipative) portion. We premultiply the flux by a shock-detecting switch, which ensures that the dissipation only occurs around shocks.[31] A fourth-order centered KEC scheme is employed for the present study. The viscous fluxes are modeled with central differences that have second-order accuracy. We perform time integration using an implicit second-order Euler method with point relaxation to maintain numerical stability.[32]

The linear system of equations (4) are discretized by fourth-order centered finite differences applied on a stretched mesh. This results in a large sparse matrix.[25] Global modes are extracted by the shift-and-invert Arnoldi method as implemented by the software package ARPACK.[33] The inversion step is computed by finding the LU decomposition of the shifted sparse matrix using the massively parallel SuperLU package.[34] We used a numerical filter to add minor amounts of scale-selective artificial dissipation to damp spurious modes associated with the smallest wavelengths allowed by the mesh. This filter does not affect the discrete modes of interest if they are well-resolved.[35] The numerical filter is introduced by adding terms of the form $\epsilon(\partial^4 \boldsymbol{q}/\partial x^4)$ and $\epsilon(\partial^4 \boldsymbol{q}/\partial y^4)$. Sponge layers are employed at the top, left, and right boundaries to absorb outgoing information with minimal reflection.[36]

III. RESULTS

A. Base flows

In order to conduct a detailed analysis of an oblique shock wave/laminar boundary layer interaction at Mach 5.92, we first need to compute several steady 2D base flows. The only parameter that changes across these base flows is the incident shock angle. We first obtain the boundary condition without the incident shock at the left inlet separately for this SWBLI by simulating a zero-pressure-gradient boundary layer developing over a flat plate.[29] Next, we introduce the incident oblique shock wave by enforcing the Rankine-Hugoniot conditions at a point along the left boundary. We select this point so that the oblique shock impinges upon the wall at a fixed distance of $119\delta^*$ from the leading edge. This ensures that the Reynolds number at the impingement point is constant for various shock angles. The bottom boundary is modeled as an adiabatic wall. We enforce a hypersonic freestream inlet along the top boundary. Lastly, we impose an outlet boundary condition along the right edge of the domain.

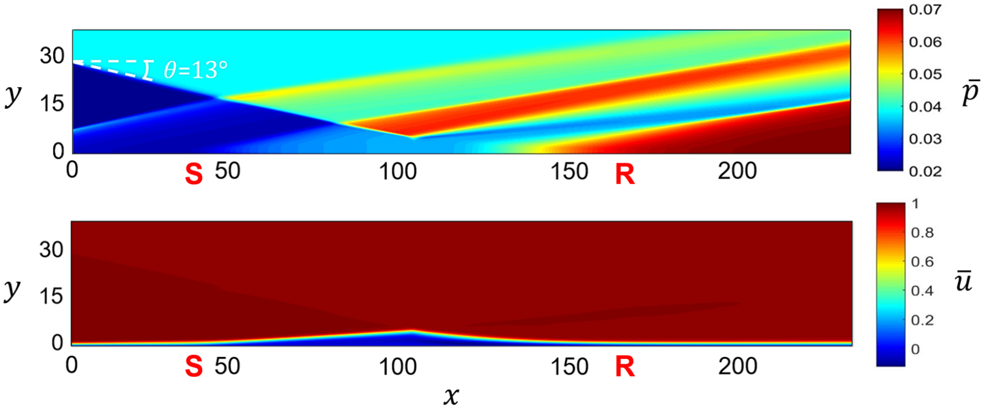

Figure 2: Contour plots of pressure and entropy for an oblique shock wave/laminar boundary layer interaction at $M_\infty = 5.92$ with an incident shock angle of $\theta = 13°$. Here, S and R represent the separation and reattachment points, respectively.

A stretched grid in the wall-normal direction with $y^+ = 0.6$ is employed to accurately capture sharp gradients associated with the thin boundary layer. Here y^+ refers to the non-dimensional wall distance in viscous units.[4] To resolve small traveling waves throughout the domain, we use uniform mesh spacing in the streamwise direction. At a single frequency, long wavelengths in the freestream are connected to short wavelengths inside the recirculation bubble because of the large velocity difference. We resolved the domain by $n_x = 998$ and $n_y = 450$ grid points in the streamwise and wall-normal directions, respectively. This resolution is sufficient according to a recent grid convergence study.[29]

We ran the base flow simulations for approximately sixty flow through times with the US3D hypersonic flow solver,[22] until the residual was on the order of machine zero. A base flow with $\theta = 13°$ is shown in Figure 2. We non-dimensionalize x, y, and z by the displacement thickness δ^*. Notice the presence of an incident shock, a bow shock, compression waves, and an expansion fan in the pressure contours. We clearly see how the boundary layer develops in the streamwise velocity contours. This case is unstable to 3D fluctuations, which we will see later. It is, however, stable for fluctuations with a spanwise wavenumber of $\beta = 0$. Therefore, by enforcing two-dimensionality upon our simulations, we can converge to an exact steady state solution to the base flow equations (1) that is unstable to small fluctuations.

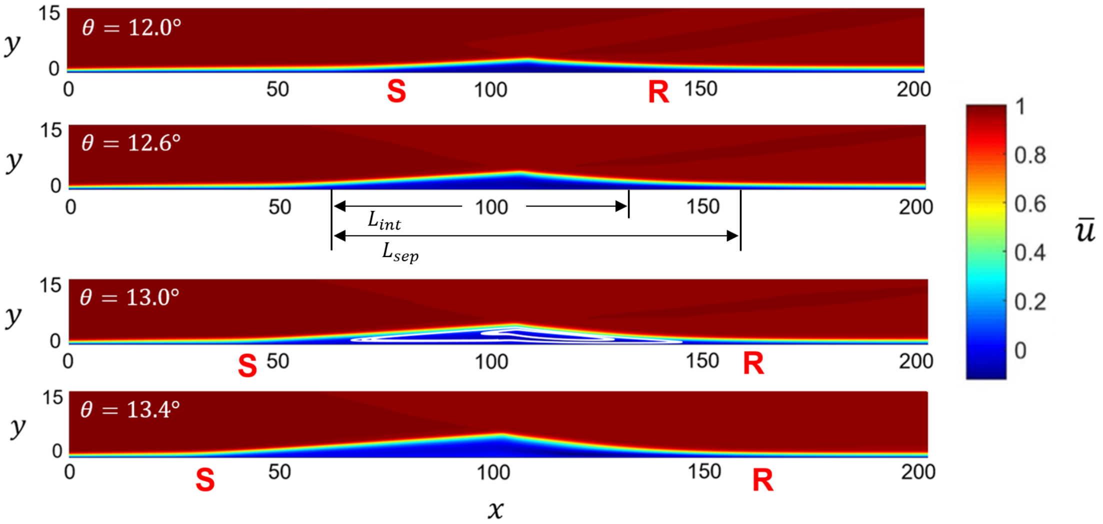

Figure 3: Contours of streamwise velocity for an oblique shock wave/laminar boundary layer interaction at $M_\infty = 5.92$ with four incident shock angles. Here, streamlines are superimposed on one of the velocity fields.

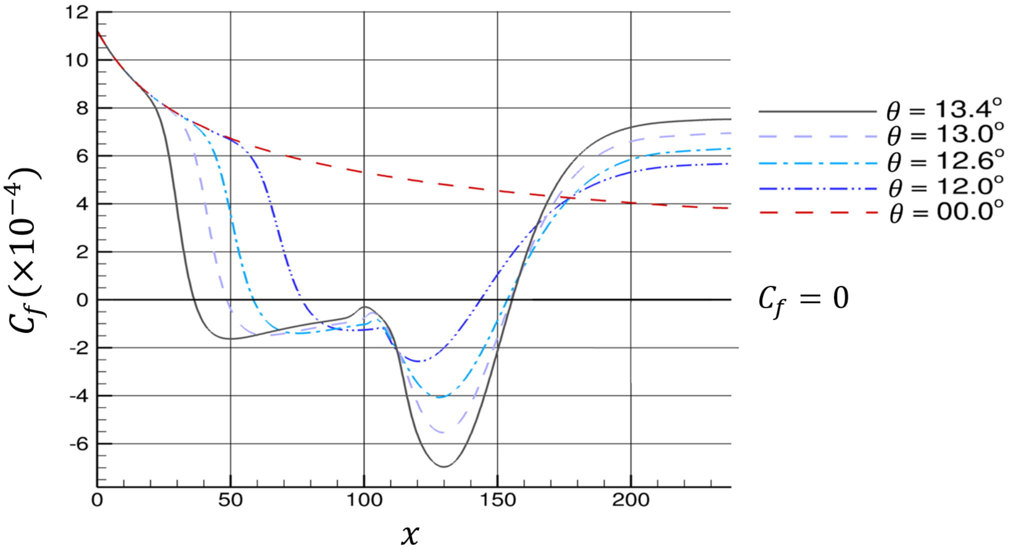

Figure 4: The skin-friction coefficient C_f in the streamwise direction located one grid point above the wall for a SWBLI at $M_\infty = 5.92$ with various incident shock angles.

To visualize how the SWBLI changes with the incident shock angle, we plot contours of streamwise velocity for several base flows in Figure 3. The recirculation bubble gets significantly larger as the incident shock angle increases from 12° to 13.4°. Here $L_{sep} = 74$ for $\theta = 12°$ and $L_{sep} = 126$ for $\theta = 13.4°$, where each quantity has been non-dimensionalized by the displacement thickness δ^*. The recirculation bubble also becomes less symmetric as the incident shock angle increases.

Figure 4 shows the wall skin-friction coefficient for a range of incident shock angles from 12° to 13.4°. Notice that the skin-friction coefficient is entirely positive inside the bubble. This is not always the case as shown in Theofilis et al.[5] for an incompressible regime. It is suggested in Rodriguez & Theofilis[6] that the presence of a secondary bubble, or negative wall skin-friction coefficient, inside the primary bubble leads to a bifurcation of the flow to a 3D steady state. We will focus our attention on incident shock angles $\theta \leq 13.4°$ and find that in the compressible regime this bifurcation occurs well before a secondary bubble forms. Here, the streamwise length of the recirculation bubble increases almost linearly with the oblique shock angle.[37]

B. Global mode analysis

To determine the critical incident shock angle at which the flow first becomes unstable, we apply global stability analysis over a range of shock angles and spanwise wavenumbers. For example, Figure 5 shows an eigenvalue spectrum resulting from global mode analysis with a shock angle of $\theta = 13°$ at a spanwise wavenumber $\beta = 0.1$. Frequencies are expressed in non-dimensional form as Strouhal numbers defined as $St = f\delta^*/U_\infty$ for this study. The real and imaginary parts of the complex frequency $St = St_r + iSt_i$ denote the temporal frequency and growth rate, respectively.

In the shift-and-invert Arnoldi method[33] used to compute the eigenvalue spectrum, shifts are positioned along the real axis to capture the least stable modes. Twenty eigenvalues are converged at each shift. We spaced shifts close together so that a portion of the spectrum converged at each shift partially overlaps with a portion converged at neighboring shifts. Modes corresponding to redundant eigenvalues extracted by nearby shifts agree well with one another, providing one check of the Arnoldi method. More eigenvalues can be found using additional shifts or increasing the number of eigenvalues sought at each shift.

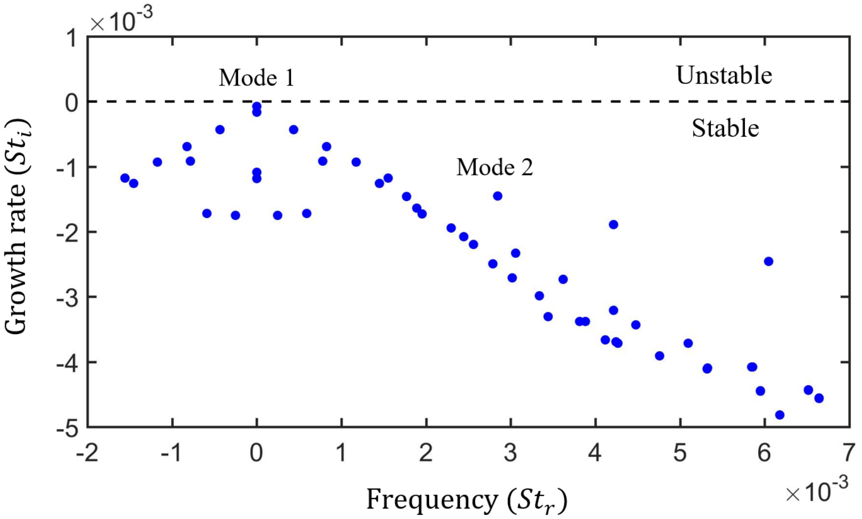

Figure 5: The eigenvalue spectrum of a SWBLI at $M_\infty = 5.92$ with an incident shock angle of $\theta = 13°$ and spanwise wavenumber $\beta = 0.1$.

Every eigenvalue in Figure 5 has a negative growth rate, which means the system is globally stable. Figure 6 displays two eigenmodes and the position of three sponge layers. Mode 1 corresponds to the least stable zero frequency eigenvalue. Notice that a significant portion of the perturbation lies within the recirculation bubble for this stationary global mode. We also see a streamwise streak that extends downstream until it gets driven to zero by the right sponge layer. Mode 2, which corresponds to an oscillatory eigenvalue, has a lot of structure within the recirculation bubble. Notice that the real streamwise velocity perturbation in global mode 2 contains positive and negative components near the front portion of the bubble. This mode is structurally similar to the other surrounding oscillatory eigenmodes (not shown). For both global modes, the long streamwise streak appears to originate near the apex of the recirculation bubble. There is also a small amount of the perturbation that surrounds a few shock waves.

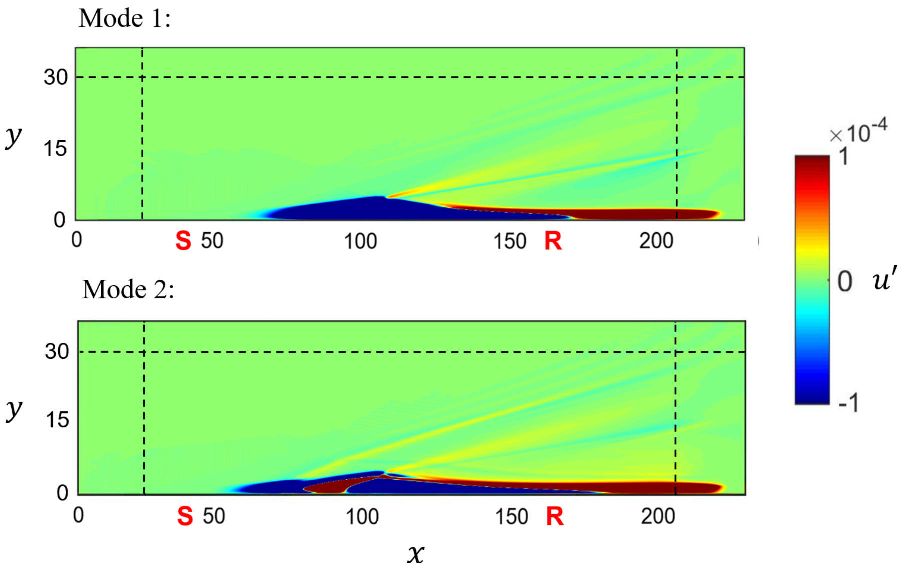

Figure 6: Stable global modes labeled in Figure 5 colored by the real part of the streamwise velocity perturbation. Here, the dashed lines indicate the start of three different sponge layers.

Next, we increase the spanwise wavenumber to $\beta = 0.25$ and repeat the same analysis, keeping the shock angle fixed at $\theta = 13°$. Figure 7 shows the eigenvalue spectrum at these conditions. We see that one stationary eigenmode has a positive growth rate, which means the system is globally unstable. Robinet[7] found a similar unstable stationary mode for an oblique shock wave/laminar boundary layer interaction at Mach 2.15. Figure 8 displays the least stable zero frequency eigenmode in 3D. This unstable global mode also contains long streamwise streaks similar to those shown in Figure 6 at a lower spanwise wavenumber. These elongated structures are still clearly coupled to the shear layer on top of the recirculation bubble. Finally, repeating global stability analysis for a spanwise wavenumber $\beta = 0.5$, we find that the eigenvalue spectrum becomes globally stable again.

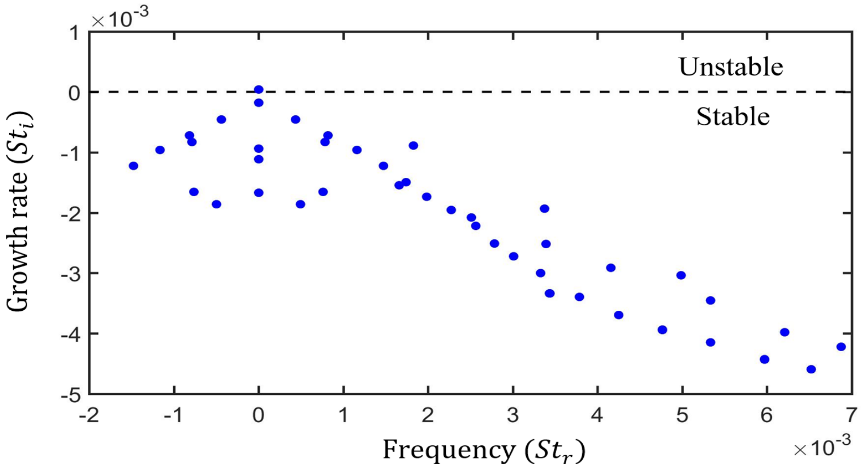

Figure 7: The eigenvalue spectrum of a SWBLI at $M_\infty = 5.92$ with an incident shock angle of $\theta = 13°$ and spanwise wavenumber $\beta = 0.25$.

While $\theta = 13°$ supported global instability over a range of spanwise wavenumbers, stability analysis of incident shock angles $\theta = 12.6°$ and $\theta = 12.8°$ revealed these cases to be globally stable at all spanwise wavenumbers. Increasing the shock angle to $\theta_{crit} = 12.9°$, however, resulted in instability at a single spanwise wavenumber $\beta_{crit} = 0.25$. Figure 9 shows the maximum growth rate versus spanwise wavenumber for angles ranging from $\theta = 12.6°$ to $\theta = 13°$. Above the critical shock angle $\theta_{crit} = 12.9°$, the 2D flow bifurcates to a 3D steady state with spanwise wavenumber $\beta_{crit} = 0.25$. The least stable global mode for every incident shock angle and spanwise wavenumber is zero frequency. Thus, the flow will never become unsteady at these conditions. We see that $\beta = 0.25$ results in the largest growth rate for every shock angle. As the spanwise wavenumber approaches zero, we expect the system to become fully stable because the base flows are 2D and the 3D component of the perturbation gets smaller. The system stabilizes for spanwise wavenumbers above $\beta = 0.5$, which has been seen before.[6,7]

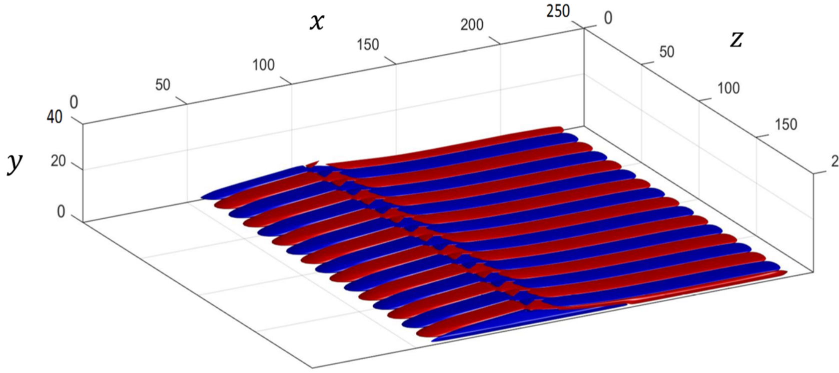

Figure 8: The unstable global mode, or more specifically $\hat{q}e^{i(0.25z)} + c.c.$, in Figure 7 visualized by the real part of the normalized, non-dimensional streamwise velocity perturbation. Red denotes a positive velocity while blue is negative.

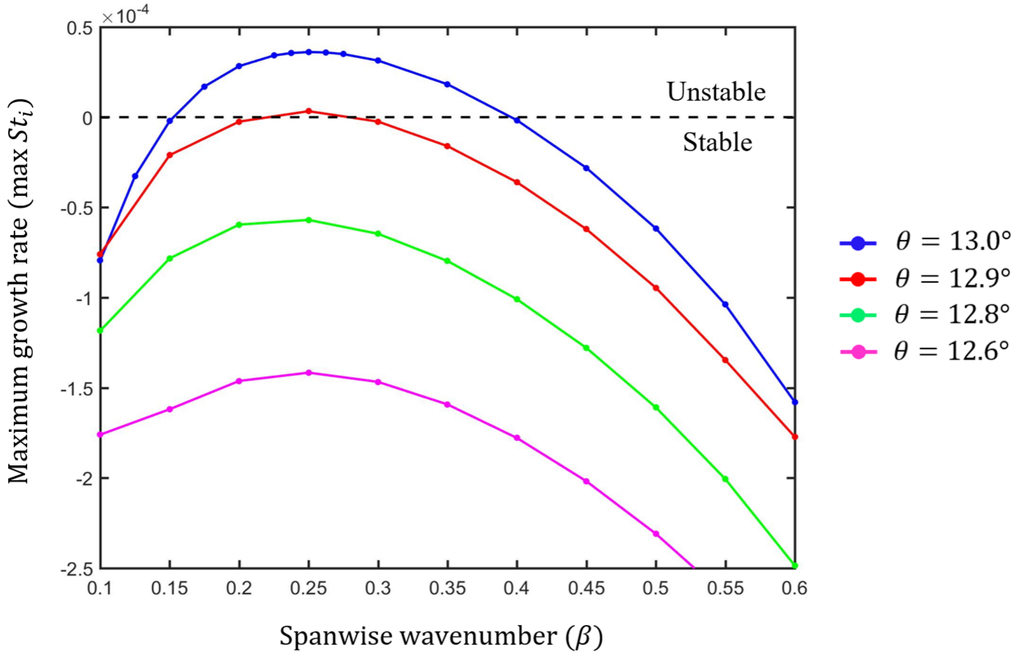

Figure 9: The maximum growth rate versus spanwise wavenumber for an oblique shock wave/laminar boundary layer interaction at $M_\infty = 5.92$ with four incident shock angles.

C. Sensitivity analysis

In the previous section, we found that the 2D oblique shock wave/boundary layer interaction bifurcates to a 3D steady state at $\theta = 12.9°$. To further interpret the physical mechanism responsible for bifurcation, we consider the sensitivity of the unstable mode to base flow modification. This also allows us to assess the robustness of our results and to understand the spatial origin of the stability modes.

First, we compute the adjoint modes to study how upstream fluctuations affect the direct global modes of the SWBLI. An adjoint eigenmode indicates where the flow is most receptive to forcing.[28] We solve the adjoint system (6b) with the continuous approach. Here integration by parts is used to derive the equations, which are then discretized. This allows for proper incorporation of the boundary conditions. Adjoint modes also allow us to quantify sensitivity of an eigenspectrum to changes in the base flow. We consider the shock angle $\theta = 13°$ with spanwise wavenumber $\beta = 0.25$ initially. Moreover, the stretched grid with $(n_x, n_y) = (998, 450)$ was again employed for this analysis. Figure 10 illustrates the unstable adjoint global mode that corresponds to the direct mode shown in Figure 8 with contours of streamwise velocity perturbation. The spatial separation of the direct and adjoint global modes shown in Figures 8 and 10 indicate significant convective non-normality. For a comprehensive discussion on non-normal operators and their properties see Schmid and Henningson.[38]

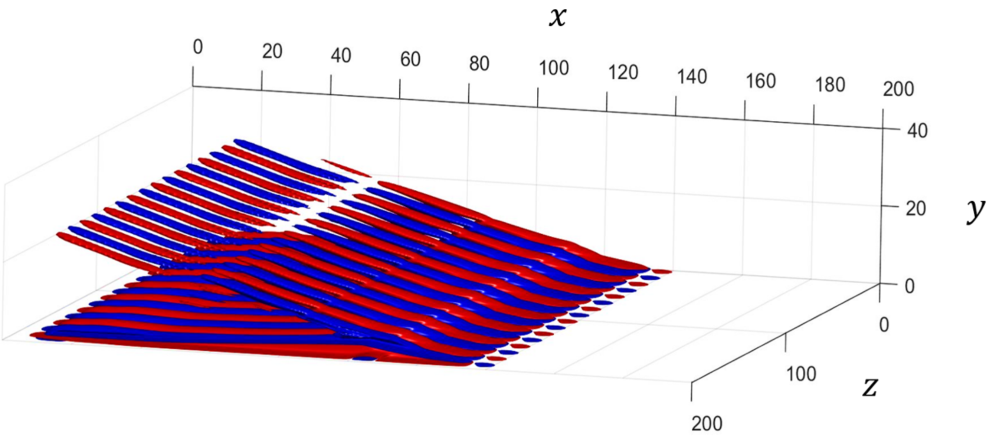

Figure 10: The unstable global mode, or more specifically $\hat{q}^{+}e^{i(0.25z)} + c.c.$, in Figure 7 visualized by the real part of the normalized, non-dimensional streamwise velocity perturbation. Red denotes a positive velocity while blue is negative.

Notice that in Figure 10 long streaks are present inside the boundary layer extending from the inlet downstream to the recirculation bubble. There is also a component of the perturbation that resides along the incident shock in the freestream. This means that the unstable eigenmode is receptive to forcing in the boundary layer and around the incident shock. We do not show the adjoint eigenvalue spectrum because it is exactly conjugate symmetric to the direct eigenvalue spectrum in Figure 7. If the grid size is adequate to resolve the small scales, then we know that the continuous adjoint and direct eigenspectra will be conjugate symmetric.[27] We see similar results for the stable global modes at $\theta = 13°$ and $\beta = 0.25$ as well as with modes at other incident shock angles and spanwise wavenumbers not shown here.

Mathematically, an upper bound for the deviation of an eigenvalue $\partial\omega_j$ associated with the linear operator A due to a structural perturbation P (such as that created by changing the base flow slightly) is given by $|\partial\omega_j| \leq ||\boldsymbol{q}'_j||_E ||P||_E ||\boldsymbol{q}^{+}_j||_E$ from Schmid and Henningson.[38] Here $\boldsymbol{q}'_j$ and $\boldsymbol{q}^{+}_j$ are the direct and adjoint eigenmodes corresponding to the deviation $\partial\omega_j$, respectively. The subscript E denotes an energy norm based on the standard definition of weighted norms.[39] Here, P has the strongest effect when $||\boldsymbol{q}'_j||_E ||\boldsymbol{q}^{+}_j||_E$ is large. In physical terms, this is the region of space where the direct and adjoint global modes overlap.[28] An eigenvalue is generally insensitive to modifications of the base flow outside this region. Therefore, we define the wavemaker as $||\boldsymbol{q}'_j||_E ||\boldsymbol{q}^{+}_j||_E$, since this quantity provides an upper boundary on the sensitivity of an eigenvalue to base flow modification.[27]

We show the wavemaker for incident shock angles ranging from $\theta = 12°$ to $\theta = 13.4°$ in Figure 11. We hold the spanwise wavenumber to a constant value of 0.25. Notice that for every case the wavemaker is located far away from the top, left, and right boundary. Therefore, any changes to the three sponge layers or domain size should not have a significant impact on the global mode dynamics. For an incident shock angle of $\theta = 12°$, we see that the wavemaker resides in the recirculation bubble. It is evenly distributed between the separation and reattachment points. As the shock angle increases to $\theta = 13.4°$, we see the wavemaker shift to the back portion of the recirculation bubble near reattachment. This behavior is directly connected to the change in symmetry of the recirculation bubble seen in Figure 3. Therefore, the bifurcation at $\theta = 12.9°$ is likely a product of the recirculation bubble and wavemaker being skewed toward reattachment. Remember that streamlines close to the recirculation bubble have significantly more curvature over the back portion than over the front for $\theta \geq 12.9°$. The wavemaker is similar for the other relevant global modes at different incident shock angles and spanwise wavenumbers. One can use structural sensitivity analysis to understand how to optimally modify the base flow inside the wavemaker to alter the stability characteristics of an oblique shock wave/laminar boundary layer interaction, but this is left to a future study.

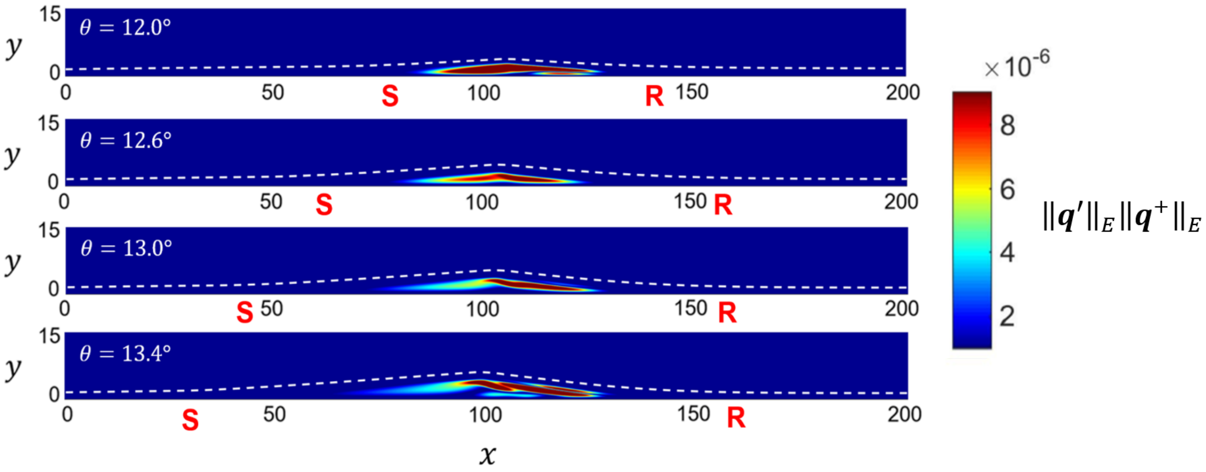

Figure 11: The wavemaker for an oblique shock wave/laminar boundary layer interaction with four incident shock angles. Every case is associated with the least stable global mode at a spanwise wavenumber of $\beta = 0.25$. A dividing streamline is superimposed on each case.

D. Görtler instability

Since the global mode shapes and base flow sensitivity analysis indicate the importance of regions in the flow where streamlines have significant curvature, we investigate Görtler instability[40] as a possible mechanism driving the bifurcation. Long streamwise streaks seen in Figures 6 and 8 also suggest the presence of Görtler vortices. To quantify this effect, we define the radius of curvature for streamlines with the expression below.[41]

$$\mathscr{R} = \frac{\|\bar{\boldsymbol{u}}\|}{\boldsymbol{\nabla}\psi \cdot (\bar{\boldsymbol{u}} \cdot \boldsymbol{\nabla}\bar{\boldsymbol{u}})} \tag{7}$$

Here, $\|\bar{\boldsymbol{u}}\|$ represents the Euclidean norm of the base flow velocity, and ψ is the streamfunction such that $\bar{\boldsymbol{u}} = \boldsymbol{\nabla} \times \boldsymbol{\psi}$ where $\boldsymbol{\psi} = [0\ 0\ \psi]$. We express the streamline curvature as $\kappa = \epsilon(x/\delta^*)/\mathscr{R}$ with ϵ denoting the viscous scale.[42] In this study, we define the Görtler number as

$$G = \sqrt{\kappa/\epsilon}. \tag{8}$$

Figure 12 shows the Görtler number G as a function of streamwise location evaluated from base flows with $\theta = 12°$, $\theta = 12.6°$, $\theta = 13°$, and $\theta = 13.4°$. This is applied to the streamline with a wall-normal distance of $1.5\delta^*$ at the inlet. For compressible flow, Görtler vortices likely become important when $G > 0.6$ according to Hall & Malik.[43] Notice in Figure 12 that the Görtler number surpasses this critical value near separation and reattachment in every base flow.

We see for $\theta = 12°$ that the Görtler number is equally large upstream and downstream of the recirculation bubble. As the incident shock angle grows, the Görtler number decreases at the separation point and increases near reattachment. This is expected because the curvature of streamlines along the back portion of the recirculation bubble increases with growing shock angle. The largest value of G is roughly 1.9, which happens near the reattachment point for $\theta = 13.4°$. Furthermore, there is a clear relationship between the asymmetry of the recirculation bubble, the position of the wavemaker, and the Görtler number. We do know that centrifugal instability is responsible for amplifying the streamwise streaks in the SWBLI. Since the Görtler number surpasses its critical value for base flows with an incident shock angle less than $\theta = 12.9°$, however, we know that Görtler instability cannot be solely responsible for the bifurcation. The formation of streamwise streaks at all shock angles, even though they are temporally damped, gives further evidence to this conclusion.

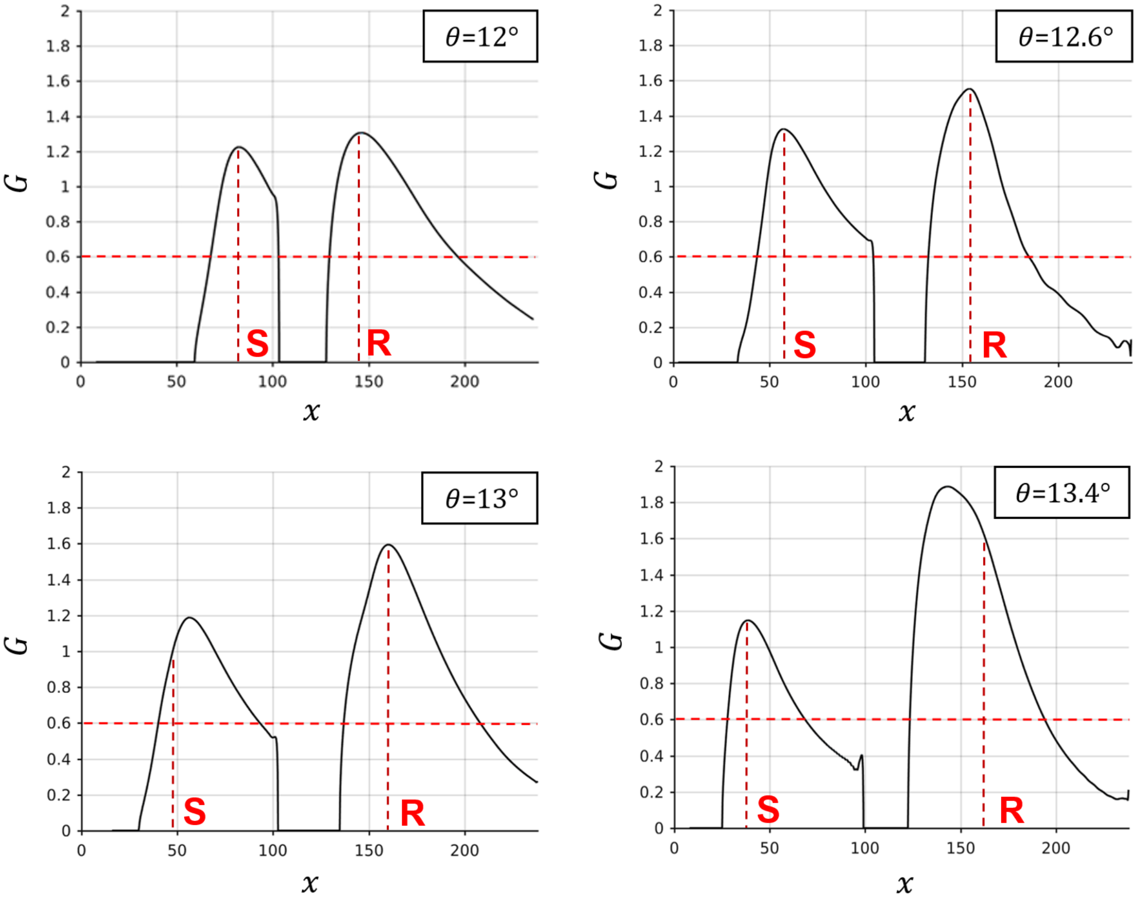

Figure 12: Plots of Görtler number versus streamwise location for several 2D base flows. We only display G when the streamlines are concave.

IV. CONCLUSIONS

An oblique shock wave impinging on a laminar boundary layer at Mach 5.92 has been investigated. We computed 2D base flows with the US3D compressible flow solver[22] at incident shock angles ranging from 12° to 13.4°. As the shock angle increases, the recirculation bubble becomes significantly larger and more asymmetric. At the largest shock angle ($\theta = 13.4°$), streamlines close to the recirculation bubble have significantly more curvature over the back portion of the bubble than over the front portion. There is a bifurcation of the initially 2D flow to a 3D steady state at $\theta_{crit} = 12.9°$. The non-dimensional spanwise wavenumber selected at this bifurcation is $\beta_{crit} = 0.25$, which we found using global stability analysis applied about the steady base flows. Long streamwise streaks that originate in the shear layer on top of the recirculation bubble are present in the unstable stationary global mode.

We compute the adjoint eigenmodes to understand how upstream fluctuations affect the direct global modes of the oblique shock wave/laminar boundary layer interaction. The spatial separation of the direct and adjoint global modes shown in Figures 8 and 10 indicate significant convective non-normality.[38] We see from Figure 10 that the unstable adjoint global mode has long streaks present inside the boundary layer extending from the inlet downstream to the recirculation bubble. There is also a component of the perturbation that resides along the incident shock in the freestream. Thus, the least stable stationary global mode is receptive to forcing in the boundary layer and along the oblique shock wave. The wavemaker is computed for incident shock angles ranging from 12° to 13.4°. For every case, the wavemaker resides in the recirculation bubble, but it shifts towards the reattachment point as the incident shock angle increases. This analysis highlighted regions of the flow with significant streamline curvature as important to the dynamics of instability.

We compute the Görtler number associated with curved streamlines taken from the base flows to assess the possibility of centrifugal instability.[13] The Görtler number surpassed its critical value near separation and reattachment for every base flow. As the oblique shock angle grows, we see the Görtler number decrease at the separation point and increase near reattachment. Furthermore, there is a distinct relationship between the asymmetry of the recirculation bubble, the position of the wavemaker, and the Görtler number. We do know that centrifugal instability is responsible for amplifying the streamwise streaks in the SWBLI. Since the Görtler number surpasses its critical value for base flows with $\theta \leq 12.9°$, we know that Görtler instability can not be solely responsible for the bifurcation.

ACKNOWLEDGMENTS

We are grateful to the Office of Naval Research for their support of this study through grant number N00014-15-1-2522. Discussions with Professor Pino Martin at the University of Maryland are appreciated.

References

[1] Délery, J. and Dussauge, J.-P., "Some physical aspects of shock wave/boundary layer interactions," *Shock Waves*, Vol. 19, 2009, pp. 453-468.

[2] Mack, L. M. , Boundary-layer stability theory, Part B, Jet Propulsion Laboratory, Pasadena, California, Document No. 900-277, 1969.

[3] Federov, A., "Transition and stability of high-speed boundary layers," *Annual Review of Fluid Mechanics*, Vol. 43, 2010, pp. 79-95.

[4] Frank M. White, *Viscous Fluid Flow*, McGraw-Hill, New York, 2006.

[5] Theofilis, V., Hein, S., and Dallmann, U., "On the origins of unsteadiness and three-dimensionality in a laminar separation bubble," *Philosophical Transactions of the Royal Society A*, Vol. 358, 2000, pp. 3229-3246.

[6] Rodriguez, D. and Theofilis, V., "Structural changes of laminar separation bubbles induced by global linear instability," *Journal of Fluid Mechanics*, Vol. 655, 2010, pp. 280-305.

[7] Robinet, J.-Ch., "Bifurcations in shock-wave/laminar-boundary-layer interaction: global instability approach," *Journal of Fluid Mechanics*, Vol. 579, 2007, pp. 85-112.

[8] Erengil, M. E. and Dolling, D. S., "Unsteady wave structure near separation in a Mach 5 compression ramp interaction," *AIAA Journal*, Vol. 29, No. 5, 1991, pp. 728-735.

[9] Ünalmis, Ö. H. and Dolling, D. S., "Decay of wall pressure field and structure of a Mach 5 adiabatic turbulent boundary layer," AIAA Paper No. 1994-2363, June 1994, pp. 1-9.

[10] Ganapathisubramani, B., Clemens, N. T., and Dolling, D. S., "Effects of upstream boundary layer on the unsteadiness of shock-induced separation," *Journal of Fluid Mechanics*, Vol. 585, 2007, pp. 369-394.

[11] Wu, M. and Martin, M. P., "Direct numerical simulation of supersonic turbulent boundary layer over a compression ramp," *AIAA Journal*, Vol. 45, No. 4, 2007, pp. 879-889.

[12] Touber, E. and Sandham, N. D., "Large-eddy simulation of low-frequency unsteadiness in a turbulent shock-induced separation bubble," *Theoretical and Computational Fluid Dynamics*, Vol. 23, No. 2, 2009, pp. 79-107.

[13] Priebe, S. and Martin, M. P., "Low-frequency unsteadiness in shock wave-turbulent boundary layer interaction," *Journal of Fluid Mechanics*, Vol. 699, 2012, pp. 1-49.

[14] Nichols, J. W., Larsson, J., Bernardini, M., and Pirozzoli, S., "Stability and modal analysis of shock/boundary layer interactions," *Theoretical and Computational Fluid Dynamics*, Vol. 30, 2016, pp. 1-18.

[15] Dupont, P., Debiève, J.-F., Dussauge, J.-P., Ardissonne, J. P., and Haddad, C., "Unsteadiness in shock wave/boundary layer interaction," Aérodynamique des Tuyères et Arrières-Corps, Technical Report, ONERA, September 2003.

[16] Piponniau, S., Dussauge, J.-P., Debiève, J.-F., and Dupont, P., "A simple model for low-frequency unsteadiness in shock-induced separation, *Journal of Fluid Mechanics*, Vol. 629, 2009, pp. 87-108.

[17] Pirozzoli, S. and Grasso, F., "Direct numerical simulation of impinging shock wave/turbulent boundary layer interaction at $M = 2.25$, *Physics of Fluids*, Vol. 18, No. 6, 2006, pp. 1-17.

[18] Sansica, A., Sandham, N. D., and Hu, Z., "Forced response of a laminar shock-induced separation bubble," *Physics of Fluids*, Vol. 26, No. 9, 2014, pp. 1-14.

[19] Clemens, N. T. and Narayanaswamy, V., "Low-frequency unsteadiness of shock wave/turbulent boundary layer interactions," *Annual Review of Fluid Mechanics*, Vol. 46, 2014, pp. 469-492.

[20] Benay, R., Chanetz, B., Mangin, B., Vandomme, L., and Perraud, J., "Shock wave/transitional boundary-layer interactions in hypersonic flow," *AIAA Journal*, Vol. 44, No. 6, 2006, pp. 1243-1254.

[21] Sandham, N. D., Schülein, E., Wagner, A., Willems, S., and Steelant, J., "Transitional shock-wave/boundary-layer interactions in hypersonic flow," *Journal of Fluid Mechanics*, Vol. 752, 2014, pp. 349-382.

[22] Candler, G. V., Subbareddy, P. K., and Nompelis, I., "CFD Methods for Hypersonic Flows and Aerothermodynamics," Hypersonic Nonequilibrium Flows: Fundamentals and Recent Advances, edited by E. Josyula, Vol 247, Progress in Astronautics and Aeronautics, AIAA, 2015, pp. 203-237.

[23] Semper, M. T., Pruski, B. J., and Bowersox, R. D. W., "Freestream turbulence measurements in a continuously variable hypersonic wind tunnel," AIAA Paper No. 2012-0732, June 2012, pp. 1-13.

[24] Sesterhenn, J., "Bifurcations in shock-wave/laminar-boundary-layer interaction: global instability approach," *Computers and Fluids*, Vol. 30, No. 1, 2000, pp. 37-67.

[25] Nichols, J. W. and Lele, S. K., "Global modes and transient response of a cold supersonic jet," *Journal of Fluid Mechanics*, Vol. 669, 2011, pp. 225-241.

[26] Luchini, P. and Bottaro, A., "Adjoint equations in stability analysis," *Annual Review of Fluid Mechanics*, Vol. 46, 2013, pp. 493-517.

[27] Marquet, O., Sipp, D., and Jacquin, L., "Sensitivity analysis and passive control of cylinder flow," *Journal of Fluid Mechanics*, Vol. 615, 2008, pp. 221-252.

[28] Chomaz, J.-M., "Global instabilities in spatially developing flows: non-normality and nonlinearity," *Annual Review of Fluid Mechanics*, Vol. 37, 2005, pp. 357-392.

[29] Shrestha, P., Dwivedi, A., Hildebrand, N., Nichols, J. W., Jovanović, M. R., and Candler, G. V., "Interaction of an oblique shock with a transitional Mach 5.92 boundary layer," AIAA Paper No. 2016-3647, June 2016, pp. 1-14.

[30] Subbareddy, P. K. and Candler, G. V., "A fully discrete, kinetic energy consistent finite-volume scheme for compressible flows," *Journal of Computational Physics*, Vol. 228, No. 5, 2009, pp. 1347-1364.

[31] Ducros, F., Ferrand, V., Nicoud, F., Weber, C., Darracq, D., Gacherieu, C., and Poinsot, T., "Large-eddy simulation of the shock/turbulence interaction," *Journal of Computational Physics*, Vol. 152, No. 2, 1999, pp. 517-549.

[32] Wright, M. J., Candler, G. V., and Bose, D., "Data-parallel line relaxation method for the NavierStokes equations," *AIAA Journal*, Vol. 36, No. 9, 1998, pp. 1603-1609.

[33] Lehoucq, R. B., Sorensen, D. C., and Yang, C., "ARPACK Users' Guide: Solution of Large-Scale Eigenvalue Problems with Implicitly Restarted Arnoldi Methods," Society for Industrial and Applied Mathematics, 1997.

[34] Li, X. S. and Demmel, J. W., "SuperLU_DIST: a scalable distributed memory sparse direct solver for unsymmetric linear systems," *ACM Transactions on Mathematical Software*, Vol. 29, No. 2, 2003, pp. 110-140.

[35] Nichols, J. W., Lele, S. K., and Moin, P., "Global mode decomposition of supersonic jet noise," Center for Turbulence Research, Annual Research Briefs, Stanford University, 2009, pp. 3-15.

[36] Mani, A., "On the reflectivity of sponge zones in compressible flow simulations," Center for Turbulence Research, Annual Research Briefs, Stanford University, 2010, pp. 117-133.

[37] Guiho, F., Alizard, F., and Robinet, J.-Ch., "Instabilities in oblique shock wave/laminar boundary-layer interactions," *Journal of Fluid Mechanics*, Vol. 789, 2016, pp. 1-35.

[38] Schmid, P. J. and Henningson, D. S., *Stability and Transition in Shear Flows*, Springer, New York, 2001.

[39] Hanifi, A., Schmid, P. J., and Henningson, D. S., "Transient growth in compressible boundary layer flow," *Physics of Fluids*, Vol. 8, 1996, pp. 826-837.

[40] Görtler, H., "On the three-dimensional instability of laminar boundary layers on concave walls," National Advisory Committee for Aeronautics Technical Memorandum No. 1375, 1940 (unpublished).

[41] Gallaire, F., Marquillie, M., and Ehrenstein, U., "Three-dimensional transverse instabilities in detached boundary layers," *Journal of Fluid Mechanics*, Vol. 571, 2007, pp. 221-233.

[42] Saric, W. S., "Görtler vortices," *Annual Review of Fluid Mechanics*, Vol. 26, 1994, pp. 379-409.

[43] Hall, P. and Malik, M. R., "The growth of Görtler vortices in compressible boundary layers," *Journal of Engineering Mathematics*, Vol. 23, 1989, pp. 239-251.